Modal and absolute thermal instability in a vertical porous layer

Modal and Absolute Thermal Instability in a Vertical Porous Layer

A. Barletta*, M. Celli

Department of Industrial Engineering, Alma Mater Studiorum Università di Bologna, Viale Risorgimento 2, 40136 Bologna, Italy

Abstract

The conduction regime in a vertical porous layer subject to a horizontal temperature gradient is studied. The boundaries are considered as isothermal, with different temperatures, and permeable to the external environment. The linear stability of this basic flow state is analysed by testing the dynamics of the normal modes of perturbation. The numerical solution of the stability eigenvalue problem leads to the determination of the neutral stability condition. Then, the evolution in time of localised wavepacket perturbations is investigated leading to the determination of the threshold to absolute instability.

Keywords: Porous medium, Linear stability, Convection, Wavepackets, Permeable boundaries, Vertical layer, Modal instability, Absolute instability

1. Introduction

The short pioneering paper by Gill [1] provides an interesting proof that natural convection cellular patterns cannot occur in a vertical porous slab bounded by isothermal impermeable walls kept at different temperatures. This result offered a serious physical argument supporting the use of insulating porous materials in buildings instead of air gaps. Indeed, the absence of a transition from a pure heat conduction regime to multicellular convection in a vertical porous slab contrasts with the emergence of such cellular patterns in a vertical fluid layer with side heating [2]. The work by Gill [1] was further developed by other authors [3–8] who extended the analysis to several aspects including the nonlinear effects and the possible lack of local thermal equilibrium between the fluid and the porous material. More recently, the study by Gill [1] has been revisited by inspecting the effects of relaxing the assumption of impermeable boundaries. Barletta [9] provided an evidence that multicellular patterns can indeed emerge in a vertical porous layer driven by a horizontal temperature gradient if the boundaries are perfectly permeable. Starting from such findings, other investigations were performed [10–13], by envisaging the presence of a horizontal throughflow, imperfectly isothermal boundaries, lack of local thermal equilibrium and non–Darcy quadratic form–drag effects in the porous medium.

Several stability analyses of convection heat transfer regarding, say, the Rayleigh–Bénard flow systems are relative to small–amplitude perturbations [14–16]. Many of them are focussed on the

*Corresponding author

Email addresses: antonio.barletta@unibo.it (A. Barletta), michele.celli3@unibo.it (M. Celli)

concept of modal instability, by regarding the linear dynamics of normal Fourier modes and their growth in time. Growing modes happen when the value of the Rayleigh number exceeds its neutral stability threshold. However, the perturbations emerging in Nature are not necessarily described by Fourier modes, but they can be modelled as localised wavepackets travelling in the streamwise direction. Even if a given wavepacket is intrinsically a linear superposition including unstable Fourier modes, it may well display a stable behaviour at large times, meaning that its amplitude can be damped when time tends to infinity [16]. On the other hand, for sufficiently large values of the Rayleigh number (generally supercritical), every wavepacket ultimately displays a growth in time. As is well–known, this concept is the basis for the definition of the threshold to absolute instability [15–22].

This study provides an analysis of the neutral stability condition and of the threshold to absolute instability in a vertical porous channel with isothermal sidewalls kept at different uniform temperatures. The analysis carried out by Barletta [9] is further developed by allowing for imperfect permeability of the boundaries. Tuning from perfect permeability to perfect impermeability is allowed by changing a dimensionless parameter γ. The other governing parameters are the Péclet number for the vertical flow and the Rayleigh number, proportional to the boundary temperature difference. The analysis is carried out by employing a numerical solution of the stability eigenvalue problem. This analysis yields the neutral stability curves and the critical Rayleigh number relative to the modal instability, namely the possibly unstable reaction to pure Fourier mode disturbances. Moreover, the threshold condition for the wavepacket instability, *viz.* the absolute instability, is captured for wide ranges of the governing parameters.

2. Preluding argument on the experimental data

The forthcoming analysis focusses on two important elements:
a) Darcy's law and the Oberbeck–Boussinesq approximation as a model of buoyant flows in porous media;
b) The distinction between modal instability and absolute instability as a tool for the analysis of the reaction of stationary flows to external disturbances.

Element a) is a cornerstone of the wider area commonly identified as convection in porous media. There are several monographs describing the feature of such a model. We refer the reader to the book by Nield and Bejan [23] for a discussion on the experimental support to the Oberbeck–Boussinesq scheme within Darcy's flow regime in porous media. The discussion of the experimental evidence for convection in porous media provided in this book becomes particularly cogent for the present analysis when it is relative to the onset of buoyancy–induced instability in a porous medium saturated by a fluid. This topic is treated in Chapter 6 of Nield and Bejan [23]. Here, we mention the classical paper by Hartline and Lister [24], where experimental evidence for the onset of the Rayleigh–Bénard instability in a porous medium is provided. Further results were discussed by Lister [25]. This paper offers a very wide comparison between multiple sets of experimental data, from different authors, supporting the theoretical predictions formulated in the pioneering papers on the modal instability in porous media by Horton and Rogers [26] and by Lapwood [27]. Lister [25] carried out two experiments regarding convection of water which saturates either a rubberized curled coconut fibre layer or a polymethylmethacrylate beads layer. Both these experiments corroborate the theoretically predicted critical Rayleigh number for the onset of the modal instability and the supercritical heat transfer rates.

Element b) originates from the need of filling the gap between theoretical predictions and unmatched experimental data, when the unstable response to external disturbances happens with a basic state displaying a net flow rate in a given direction. The duality of modal and absolute instability is predicted theoretically to model what is actually measured by an observer in a rest reference frame while monitoring the transition to instability in a flowing fluid. The conceptual framework of absolute instability blooms in plasma physics [28, 29], but it soon finds interesting applications in fluid mechanics [15, 17, 30]. Experimental support to the theoretical predictions for the absolute instability of an axisymmetric heated air–jet discharging into cold stagnant air was found by Monkewitz et al. [31]. Lingwood [32] studied experimentally the transition to absolute instability in the boundary layer flow over a disk rotating in a still air environment. The extension to porous media flows of the absolute instability concept is definitely more recent. However, an experimental validation of the absolute instability approach to the analysis of flow in a porous medium was reported by Delache et al. [33]. By employing the absolute instability methodology, these authors were able to improve the experimental/theoretical data comparison for the transition to instability of the horizontal flow in a porous layer heated from below.

3. Governing equations

Let us consider a vertical plane porous channel with infinite height, finite transverse width L and finite spanwise width H. We set the Cartesian coordinates (x, y, z) so that x is the transverse horizontal coordinate such that $-L/2 \leqslant x \leqslant L/2$, y is the spanwise horizontal coordinate such that $0 \leqslant y \leqslant H$ and z is the vertical unbounded coordinate. Uniform temperatures T_1 and T_2, with $T_2 > T_1$, are prescribed at the boundaries $x = -L/2$ and $x = L/2$, respectively. Furthermore, the laterally confining boundaries at $y = 0$ and $y = H$ are assumed to be thermally insulated and impermeable.

The boundaries at $x = \pm L/2$ are permeable to external fluid reservoirs. These reservoirs are subject to a vertical pressure gradient given by the constant $-\Delta p/L$.

3.1. Dimensionless analysis

A scaling of the dimensional quantities is defined in order to formulate the flow problem in dimensionless terms,

$$\frac{\mathbf{u}}{\alpha/L} = \frac{(u,v,w)}{\alpha/L} \to (u,v,w) = \mathbf{u}, \qquad \frac{T-T_0}{T_2-T_1} \to T, \qquad \frac{p}{\mu\alpha/K} \to p,$$
$$\frac{(x,y,z)}{L} \to (x,y,z), \qquad \frac{t}{L^2/\alpha} \to t, \tag{1}$$

where p denotes the local difference between the pressure and the hydrostatic pressure, here called pressure for the sake of brevity, (u, v, w) are the Cartesian components of the seepage velocity $\mathbf{u}$, T is the temperature and T_0 is its reference value, $T_0 = (T_1 + T_2)/2$, α is the average thermal diffusivity, μ is the dynamic viscosity, and K is the permeability of the porous medium.

3.2. Local balance equations

The porous medium is considered as both isotropic and homogeneous, and saturated by a Newtonian fluid. Conditions of local thermal equilibrium and negligible viscous dissipation are assumed. Moreover, the thermal buoyancy is modelled through the Oberbeck–Boussinesq approximation with

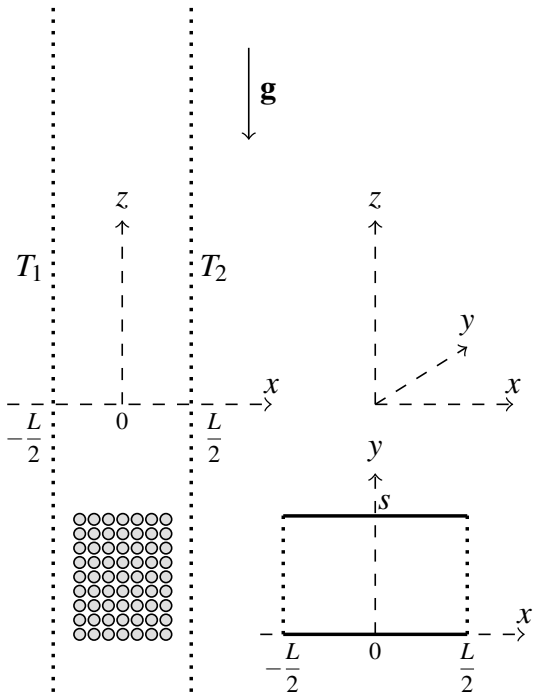

Figure 1: Reference frame and sketch of the vertical and horizontal cross–sections of the porous channel

the momentum transfer described by Darcy's law [23]. Then, the dimensionless governing equations expressing the local balances of mass, momentum and energy are written as

$$\boldsymbol{\nabla} \cdot \mathbf{u} = 0, \tag{2a}$$

$$\mathbf{u} = -\boldsymbol{\nabla} p + Ra\, T\, \hat{\mathbf{e}}_z, \tag{2b}$$

$$\sigma \frac{\partial T}{\partial t} + \mathbf{u} \cdot \boldsymbol{\nabla} T = \nabla^2 T, \tag{2c}$$

where Ra is the Darcy–Rayleigh number defined as

$$Ra = \frac{g\beta(T_2 - T_1)KL}{\nu\alpha}, \tag{3}$$

the unit vector along the z axis is $\hat{\mathbf{e}}_z$, the modulus of the gravitational acceleration $\mathbf{g}$ is g, while β is the coefficient of thermal expansion and ν the kinematic viscosity of the fluid. Finally, σ expresses the heat capacity ratio, namely the ratio between the heat capacity per unit volume of the saturated porous medium and the heat capacity per unit volume of the fluid.

3.3. Boundary conditions

The boundary conditions are given by

$$\begin{aligned} &p \pm \gamma \frac{\partial p}{\partial x} = -Pe\, z, \quad T = \pm\frac{1}{2} \quad \text{if} \quad x = \pm\frac{1}{2}, \\ &\frac{\partial p}{\partial y} = 0, \quad \frac{\partial T}{\partial y} = 0 \quad \text{if} \quad y = 0, \quad y = s, \end{aligned} \tag{4}$$

where $s = H/L$ is the aspect ratio of the channel cross–section and $Pe = K\Delta p/(\mu\alpha)$ is the Péclet number associated with the external vertical pressure gradient, $-\Delta p/L$. We point out that the condition $\hat{\mathbf{e}}_n \cdot \boldsymbol{\nabla} p = 0$, where $\hat{\mathbf{e}}_n$ is the unit vector normal to a given vertical plane boundary, expresses the impermeability of that boundary as a consequence of Darcy's law. On the other hand, $p = -Pe\, z$ yields the continuity of the boundary pressure to the pressure of the external fluid reservoir, hence, it models the perfect permeability of the boundary. In other words, equation (4) implies that the dimensionless parameter $\gamma > 0$ modulates the imperfect permeability of the boundaries at $x = \pm 1/2$, including the limiting cases $\gamma \to 0$ (perfect permeability) and $\gamma \to \infty$ (impermeability). As a result, third kind (or Robin) boundary conditions on the pressure p are assigned at $x = \pm\, 1/2$. A detailed description of the pressure boundary conditions is provided in Appendix A.

We mention that a diversely formulated model of the velocity condition at a permeable boundary is described and adopted in a paper by Nygård and Tyvand [34].

3.4. Basic mixed convection flow

A stationary parallel flow solution of equations (2) and (4) exists, given by

$$u_b = 0, \quad v_b = 0, \quad w_b = Pe + Ra\, x, \quad p_b = -Pe\, z, \quad T_b = x. \tag{5}$$

We employed the subscript "b" to denote the basic flow. We also note that, on account of equation (5), the Péclet number yields the flow rate across the channel, namely

$$\int_{-1/2}^{1/2} w_b \, \mathrm{d}x = Pe. \tag{6}$$

3.5. Pressure–temperature formulation

Equations (2) can be rewritten in a different way by evaluating the divergence of equation (2b) and by taking into account equation (2a),

$$\nabla^2 p = Ra \frac{\partial T}{\partial z}, \tag{7a}$$

$$\sigma \frac{\partial T}{\partial t} - \boldsymbol{\nabla} p \cdot \boldsymbol{\nabla} T + Ra\, T \frac{\partial T}{\partial z} = \nabla^2 T. \tag{7b}$$

Equations (7), together with equation (4), provide a pressure–temperature formulation of the flow problem.

4. The dynamics of linear perturbations

The perturbations acting on the basic flow given by equation (5) are expressed as

$$p = p_b + \varepsilon\, P, \quad T = T_b + \varepsilon\, \theta. \tag{8}$$

By a standard linearisation, substitution of equation (8) into equations (4) and (7) yields

$$\nabla^2 P - Ra\,\frac{\partial \theta}{\partial z} = 0, \tag{9a}$$

$$\nabla^2 \theta - \sigma \frac{\partial \theta}{\partial t} - (Pe + Ra\,x)\,\frac{\partial \theta}{\partial z} + \frac{\partial P}{\partial x} = 0, \tag{9b}$$

$$P \pm \gamma\,\frac{\partial P}{\partial x} = 0, \quad \theta = 0 \quad \text{if} \quad x = \pm\frac{1}{2},$$

$$\frac{\partial P}{\partial y} = 0, \quad \frac{\partial \theta}{\partial y} = 0 \quad \text{if} \quad y = 0, \quad y = s. \tag{9c}$$

In fact, the perturbation parameter ε has been assumed to be so small that terms $O\big(\varepsilon^2\big)$ have been considered as negligible.

4.1. Spanwise Fourier modes

We can expand the solution of equations (9) by employing the Fourier series,

$$P(x,y,z,t) = \sum_{n=0}^{\infty} P_n(x,z,t)\,\cos\Big(\frac{n\pi y}{s}\Big),$$

$$\theta(x,y,z,t) = \sum_{n=0}^{\infty} \theta_n(x,z,t)\,\cos\Big(\frac{n\pi y}{s}\Big). \tag{10}$$

Equation (10) implies that the boundary conditions (9c) at $y = 0$ and $y = s$ are satisfied. If we substitute equation (10) into equations (9), we obtain

$$\frac{\partial^2 P_n}{\partial x^2} + \frac{\partial^2 P_n}{\partial z^2} - \Big(\frac{n\pi}{s}\Big)^2 P_n - Ra\,\frac{\partial \theta_n}{\partial z} = 0, \tag{11a}$$

$$\frac{\partial^2 \theta_n}{\partial x^2} + \frac{\partial^2 \theta_n}{\partial z^2} - \Big(\frac{n\pi}{s}\Big)^2 \theta_n - \sigma\frac{\partial \theta_n}{\partial t} - (Pe + Ra\,x)\,\frac{\partial \theta_n}{\partial z} + \frac{\partial P_n}{\partial x} = 0, \tag{11b}$$

$$P_n \pm \gamma\,\frac{\partial P_n}{\partial x} = 0, \quad \theta_n = 0 \quad \text{if} \quad x = \pm\frac{1}{2}, \tag{11c}$$

for each mode with $n = 0, 1, 2, \ldots$.

4.2. Fourier transformed governing equations

We can employ the Fourier transform for equations (11). We thus define

$$\tilde{P}_{n,k}(x,t) = \frac{1}{\sqrt{2\pi}} \int_{-\infty}^{\infty} P_n(x,z,t)\,e^{-i\,kz}\,\mathrm{d}z,$$

$$\tilde{\theta}_{n,k}(x,t) = \frac{1}{\sqrt{2\pi}} \int_{-\infty}^{\infty} \theta_n(x,z,t)\,e^{-i\,kz}\,\mathrm{d}z, \tag{12}$$

so that the inversion formula yields

$$P_n(x,z,t) = \frac{1}{\sqrt{2\pi}} \int_{-\infty}^{\infty} \tilde{P}_{n,k}(x,t)\,e^{i\,kz}\,\mathrm{d}k,$$

$$\theta_n(x,z,t) = \frac{1}{\sqrt{2\pi}} \int_{-\infty}^{\infty} \tilde{\theta}_{n,k}(x,t)\,e^{i\,kz}\,\mathrm{d}k. \tag{13}$$

By employing equation (12), the transformed equations (11) are written as

$$\frac{\partial^2 \tilde{P}_{n,k}}{\partial x^2} - \left[k^2 + \left(\frac{n\pi}{s}\right)^2\right]\tilde{P}_{n,k} - i\,kRa\,\tilde{\theta}_{n,k} = 0, \tag{14a}$$

$$\frac{\partial^2 \tilde{\theta}_{n,k}}{\partial x^2} - \left[k^2 + \left(\frac{n\pi}{s}\right)^2 + i\,k(Pe + Ra\,x)\right]\tilde{\theta}_{n,k} - \sigma\frac{\partial \tilde{\theta}_{n,k}}{\partial t} + \frac{\partial \tilde{P}_{n,k}}{\partial x} = 0, \tag{14b}$$

$$\tilde{P}_{n,k} \pm \gamma\,\frac{\partial \tilde{P}_{n,k}}{\partial x} = 0, \quad \theta_{n,k} = 0 \quad \text{if} \quad x = \pm\frac{1}{2}. \tag{14c}$$

4.3. Stability eigenvalue problem

Time dependence can be easily factorised by setting

$$\tilde{P}_{n,k}(x,t) = f(x)\,e^{\lambda t}, \quad \tilde{\theta}_{n,k}(x,t) = h(x)\,e^{\lambda t}, \tag{15}$$

where the complex growth rate λ has a direct physical meaning. Its real part λ_r is the actual growth rate of each Fourier mode, so that $\lambda_r > 0$ means modal instability, while $\lambda_r \leq 0$ means modal stability. The threshold $\lambda_r = 0$ describes the neutral stability condition. The imaginary part of λ, denoted by λ_i, coincides with $-\omega$, where ω is the angular frequency of the Fourier mode. Hence, equations (14) and (15) yield

$$f'' - \left[k^2 + \left(\frac{n\pi}{s}\right)^2\right]f - i\,kRa\,h = 0, \tag{16a}$$

$$h'' - \left[k^2 + \left(\frac{n\pi}{s}\right)^2 + i\,k(Pe + Ra\,x) + \sigma\lambda\right]h + f' = 0, \tag{16b}$$

$$f \pm \gamma\,f' = 0, \quad h = 0 \quad \text{if} \quad x = \pm\frac{1}{2}. \tag{16c}$$

Here, the primes denote derivatives for a function of one variable. Equations (16) define the stability eigenvalue problem, where (f, h) is the eigenfunction while λ is the eigenvalue.

4.4. A comment on the terminology

The forthcoming analysis of the linear instability will be carried out by distinguishing two scenarios. The first scenario is when the perturbation acting upon the basic flow state is a single Fourier mode, having a given wavenumber k. The second scenario is when the instability is triggered by a localised wavepacket, expressed through equations (10) and (13). The traditional term used for the first scenario is *convective instability*, while *absolute instability* is employed for the second scenario [15, 18]. In the present study, we prefer the term *modal instability* instead of convective instability just to avoid any confusion with the heat transfer mechanism of convection which, in the currently studied problem, is always present even under stability conditions.

5. Modal instability

The study of the conditions for the onset of modal instability starts from the analysis of equations (16). One has to identify when, for a prescribed (n, k)–mode, the growth rate λ_r changes from negative to positive, thus detecting the transition from stability to instability of that (n, k)–mode. The concept of modal instability is all based on the growth rate of a single (n, k)–mode. The time growth of the wavepackets (13) is a different matter as it deals with the absolute instability. The latter will be discussed in detail later on in this paper.

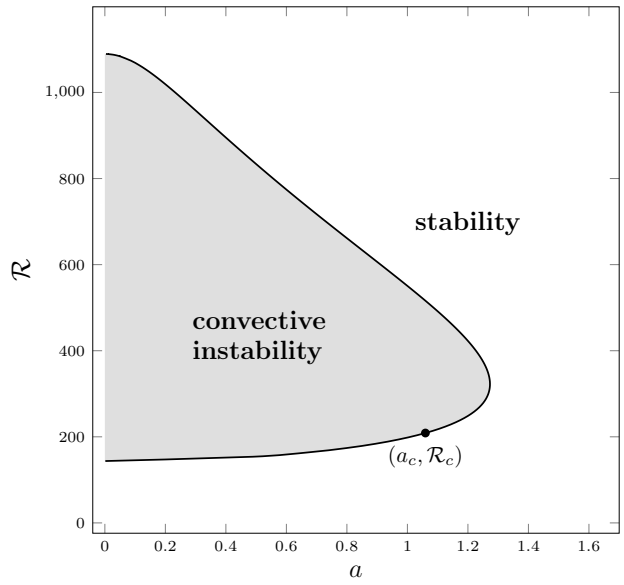

Figure 2: Modal stability map for $\gamma = 0$. The black dot identifies the critical conditions, $a = a_c$ and $\mathcal{R} = \mathcal{R}_c$, relative to the modes with $r = 0$.

5.1. A Squire transformation

A Squire transformation of equations (16) can be employed in order to reduce the number of governing parameters [9]. One can define

$$a = \sqrt{k^2 + r^2}, \quad r = \frac{n\pi}{s}, \quad S = \frac{k}{a}\,Ra, \quad \xi = \sigma\omega - kPe. \tag{17}$$

In order to detect the neutral stability condition, we fix $\lambda_r = 0$. Therefore, on account of equation (17), equations (16) can be rewritten as

$$f'' - a^2 f - i\,a\,S\,h = 0, \tag{18a}$$
$$h'' - \left[a^2 + i\,(a\,S\,x - \xi)\right]h + f' = 0, \tag{18b}$$
$$f \pm \gamma\,f' = 0, \quad h = 0 \quad \text{if} \quad x = \pm\frac{1}{2}. \tag{18c}$$

5.2. An alternative scaling

A convenient way to represent the threshold to modal instability ($\lambda_r = 0$) is by defining the quantity

$$\mathcal{R} = k\,Ra = a\,S. \tag{19}$$

Hence, equations (18) can be written as

$$f'' - a^2 f - i\,\mathcal{R}\,h = 0, \tag{20a}$$
$$h'' - \left[a^2 + i\,(\mathcal{R}\,x - \xi)\right]h + f' = 0, \tag{20b}$$
$$f \pm \gamma\,f' = 0, \quad h = 0 \quad \text{if} \quad x = \pm\frac{1}{2}. \tag{20c}$$

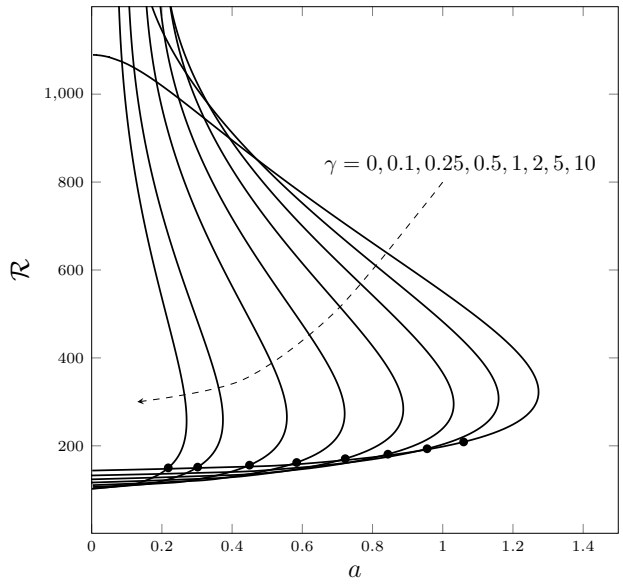

Figure 3: Neutral stability curves for different values of γ; black dots identify the critical condition, $(a_c, \mathcal{R}_c)$, relative to the modes with $r = 0$.

By solving numerically equations (20), neutral stability curves can be drawn in the $(a, \mathcal{R})$ plane for every given value of γ in order to illustrate the loci where $\lambda_r = 0$. We note that, in order to determine the critical Rayleigh number, Ra_c, and wavenumber, k_c, we have to minimise Ra as a function of k along the neutral stability curve. Thus, we must set the condition $\partial Ra/\partial k = 0$, which can be reformulated as

$$\frac{\partial \mathcal{R}}{\partial a} - \frac{a}{k^2}\,\mathcal{R} = 0, \tag{21}$$

by utilising equation (17). We mention that, only in the case $r = 0$, the critical condition $k = k_c$ and $S = S_c$ can be sought by minimising S as a function of a along a neutral stability curve.

The numerical solution of equations (20) is achieved by employing the shooting method. Extensive analyses of this method utilised for instability eigenvalue problems can be found in Straughan [35] and in Barletta [16]. In Barletta [16], a detailed description of *Octave* scripts devoted to the evaluation of the neutral stability data, as well as of the critical condition for the onset of the instability, is also provided. Just the same methodology is adopted here, so that we refer the reader to these books for further details.

The first important aspect to be highlighted here is that the neutral stability data found for different values of γ always yield $\xi = 0$. In other words, the reduced angular frequency evaluated in the comoving reference frame, defined by equation (17), is zero. This result is a strong argument of numerical nature, in the absence of a rigorous formal proof, supporting the validity of the principle of exchange of stabilities [14] in the comoving reference frame.

With reference to the case $\gamma = 0$, which means perfectly permeable boundaries, Fig. 2 shows the regions of stability and instability, separated by the neutral stability curve. The map is in the $(a, \mathcal{R})$ plane. The main feature of the instability region is that it is bounded with the minimum

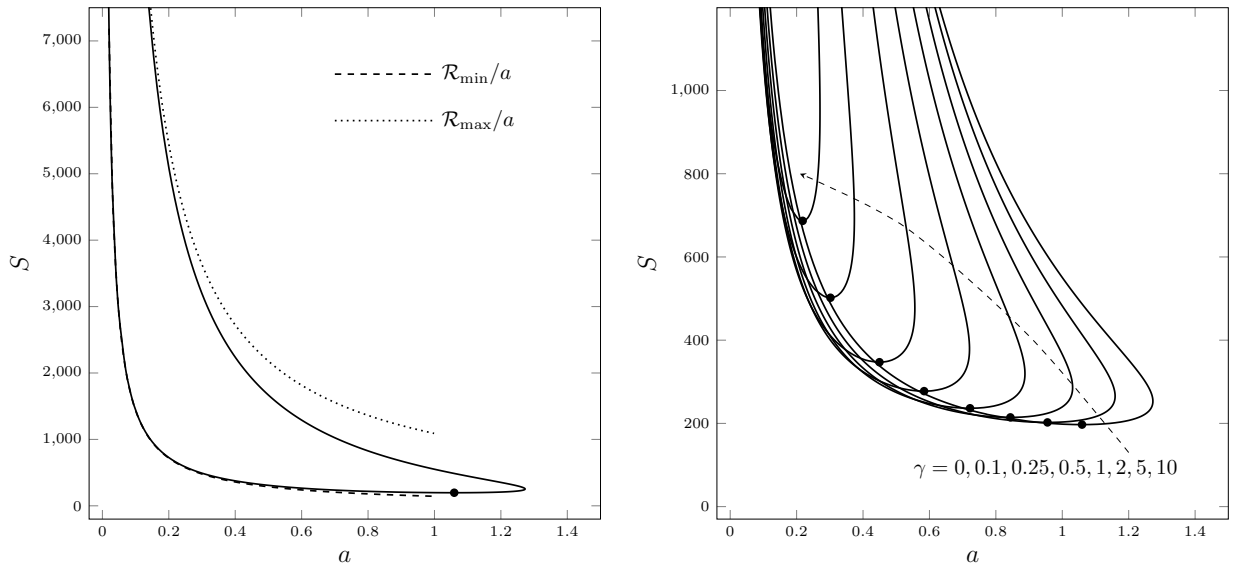

Figure 4: Left hand frame: neutral stability curve for $\gamma = 0$ compared with the asymptotic curves defined by equation (23). Right hand frame: neutral stability curves for different values of γ. The black dots denote the critical points (a_c, S_c) for $r = 0$ on each curve.

and maximum $\mathcal{R}$ points being settled at $a = 0$,

$$\mathcal{R}_{\min} = 143.7029, \quad \mathcal{R}_{\max} = 1089.380. \tag{22}$$

Equations (19) and (22) imply that the large–S behaviour of the neutral stability condition can be described through the asymptotic formulas

$$S \approx \frac{\mathcal{R}_{\min}}{a} = \frac{143.7029}{a}, \quad S \approx \frac{\mathcal{R}_{\max}}{a} = \frac{1089.380}{a}. \tag{23}$$

The critical condition $(a_c, \mathcal{R}_c)$ is determined by imposing equation (21) thus leading, for the modes with $r = 0$, to the values

$$a_c = 1.059498, \quad \mathcal{R}_c = 208.8072, \quad S_c = \frac{\mathcal{R}_c}{a_c} = 197.0812. \tag{24}$$

The values of (a_c, S_c) reported in equation (24) perfectly agree with those found by Barletta [9].

Figure 3 shows the neutral stability curves in the $(a, \mathcal{R})$ plane relative to values of γ increasing above zero. The main feature displayed in this figure is that, when $\gamma > 0$, the instability region becomes unbounded so that there exists an $\mathcal{R}_{\min}$, but not an $\mathcal{R}_{\max}$. Moreover, as γ increases, the instability region tends to become a narrower and narrower strip close to the line $a = 0$ and eventually, when $\gamma \to \infty$, this region disappears. This inference agrees with the theorem of stability proved in the paper by Gill [1]. Black dots are reported in Fig. 3 identifying the critical condition, $(a_c, \mathcal{R}_c)$, for the modes with $r = 0$ and for given values of γ. Such critical point migrates leftward in the $(a, \mathcal{R})$ plane, as γ increases.

Figure 4 shows the neutral stability data previously employed in Figs. 2 and 3 plotted in the (a, S) plane. The left hand frame illustrates the case of perfectly permeable boundaries ($\gamma = 0$),

γ	a_c	S_c	$\mathcal{R}_c$	$\mathcal{R}_{\min}$
0.1	0.9554816	202.3478	193.3396	132.6872
0.25	0.8437594	214.4592	180.9519	123.8964
0.5	0.7222494	236.3743	170.7212	116.6637
1.0	0.5839582	277.5283	162.0650	110.5742
2.0	0.4495026	347.0725	156.0100	106.3383
5.0	0.3018431	501.9864	151.5212	103.2145
10.0	0.2181754	686.7910	149.8409	102.0494
20.0	0.1560460	954.5975	148.9611	101.4404
50.0	0.0993861	1493.364	148.4197	101.0660
100.0	0.0704428	2104.359	148.2370	100.9396
1000.0	0.0223236	6632.944	148.0715	100.8253

Table 1: Critical values of (a, S) for $r = 0$ and of $\mathcal{R}_{\min}$ for $\gamma > 0$.

where a comparison with the large–S behaviour given by equation (23) is provided through the dashed and dotted lines. These asymptotic trends turn out to be fairly reliable especially for the lowest branch, $S = \mathcal{R}_{\min}/a$. The plot in the (a, S) plane evidences the minimum S feature of the critical condition (a_c, S_c) for $r = 0$. The right hand frame of Fig. 4 reveals that an increasing γ means a stabilization of the basic flow, with the neutral stability curves gradually moving upward. The black dots indicate the position of the critical point (a_c, S_c) for each γ and $r = 0$. Such minimum–S points move upward and leftward, showing that the onset of the instability requires larger and larger Rayleigh numbers, together with larger and larger wavelengths. Eventually, the limit $\gamma \to \infty$ describing the impermeable boundaries does not admit any instability, namely $S_c \to \infty$ as rigorously proved by Gill [1].

Table 1 reports numerical values of a_c, S_c and $\mathcal{R}_{\min}$ versus γ for $r = 0$. These data confirm that the gradual change from perfect permeability to perfect impermeability of the boundaries (γ increasing from to zero to infinity) yields a stabilisation of the basic flow. The values of $\mathcal{R}_{\min}$ yield an asymptotic evaluation of the product $S\,a$ along the left hand branch of the neutral stability curve, when $S \gg 1$.

Figure 5 shows the critical values of a, S, $\mathcal{R}$ versus γ for $r = 0$. An interesting feature displayed by Fig. 5, and shown also by the data reported in Table 1, is that $\mathcal{R}_c$ attains an asymptotic value when γ tends to infinity. In fact, the scaling of a_c and S_c is with $\sqrt{\gamma}$ so that the numerical data allow one to deploy the asymptotic formulas for $\gamma \gg 1$,

$$a_c \simeq \frac{0.706}{\sqrt{\gamma}}, \quad S_c \simeq 210\sqrt{\gamma}, \quad \mathcal{R}_c \simeq 148. \tag{25}$$

The asymptotic trends given by equation (25) turn out to be in excellent agreement with the plots of S_c and a_c versus γ for $r = 0$ displayed in Fig. 5, in particular when $\gamma > 10$.

Out of the Squire transformed parameters (a, S), the transition to modal instability is to be judged from the primary parameters (k, Ra) assuming that n and s or, alternately, r is prescribed. In the case $r = 0$, the pair (a, S) coincides with (k, Ra) meaning that Ra_c coincides with S_c. For a given $r > 0$, from equation (17), we have $k/a < 1$ and, hence, $Ra > S$. Thus, the modes with $r > 0$ are more stable than those with $r = 0$. The conclusion is that the modal instability occurs with $n = 0$ at its onset, whenever a finite s is prescribed. We point out that $r = 0$ has the twofold

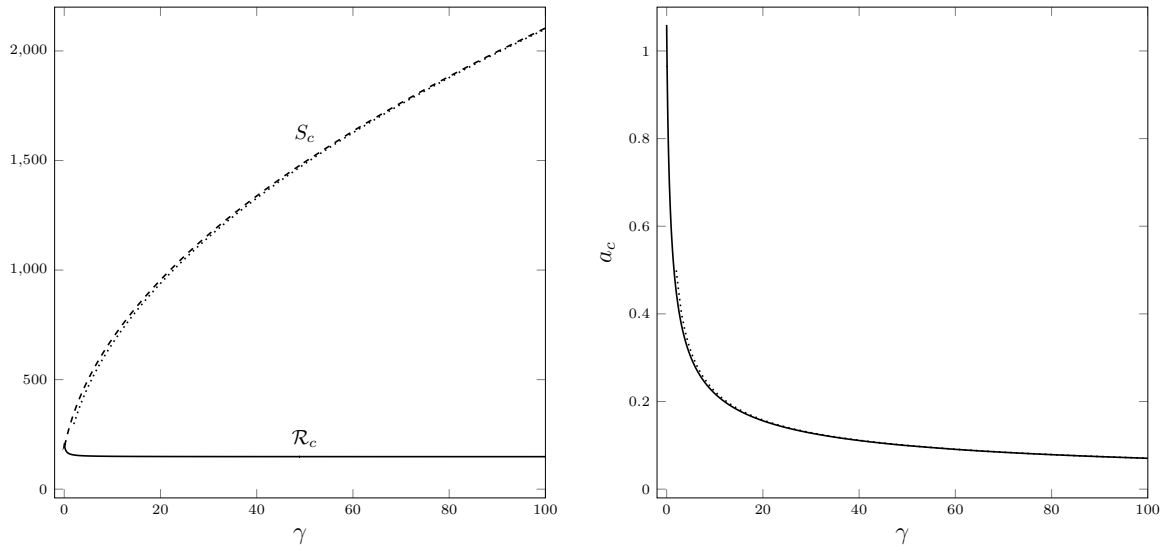

Figure 5: Left hand frame: plots of $\mathcal{R}_c$ and S_c versus γ for $r = 0$. Right hand frame: plots of a_c versus γ for $r = 0$. The dotted lines correspond to the asymptotic trends defined by equation (25).

meaning of $n = 0$ with a finite s, or $n > 0$ with $s \to \infty$, *i.e.*, no spanwise lateral confinement. On the other hand, a fixed $r > 0$ may signify many different situations where n is a nonzero integer and the aspect ratio s is finite. Hence, when s is finite, the most unstable modes are those with $n = 0$. This is the reason why we do not investigate any further the determination of the critical condition, $k = k_c$ and $Ra = Ra_c$, for the modes with $r > 0$.

Figure 4 suggests that, for every value of γ, there is a maximum value $a = a_{\max}$, such that no modal instability is detected when $a > a_{\max}$. As pointed out by Barletta [9], when $\gamma = 0$, we have

$$a_{\max} = 1.27291. \tag{26}$$

Then, if $r > a_{\max}$, we cannot have any modal instability. For example, if $\gamma = 0$ and $s = 5$, we can have unstable modes with $n = 0, 1$ and 2 while, if $\gamma = 0$ and $s = 3$, unstable modes exist only with $n = 0$ and 1. Table 2 yields some values of $a_{\max}$ and Ra_c for different values of r and γ.

6. Absolute instability

After having discussed the stable/unstable behaviour of single Fourier modes, we will now investigate the dynamics of wavepacket perturbations, expressed by the integrals introduced in equation (13). Wavepackets may be unstable when $Ra > Ra_c$, *i.e.*, the transition to absolute instability is supercritical. In other words, there exists a threshold $Ra = Ra_a$, with $Ra_a \geq Ra_c$, such that all wavepacket perturbations are unstable when $Ra > Ra_a$. Here, the subscript "a" is meant to denote the onset of unstable wavepacket perturbations, well–known in the literature as absolute instability.

The method employed to evaluate Ra_a is the steepest–descent approximation [16, 36] for wavepacket perturbations. The steepest–descent approximation is a very powerful method as it

γ	$a_{\max}$	Ra_c $[r=0]$	Ra_c $[r=0.5]$	Ra_c $[r=1]$
0	1.272911	197.0812	221.8501	368.2497
0.25	1.031145	214.4592	260.2111	1147.807
0.5	0.887615	236.3743	311.0859	—
1	0.720655	277.5283	440.4734	—
2	0.556062	347.0725	1011.948	—
5	0.373920	501.9864	—	—
10	0.270385	686.7910	—	—
20	0.193424	954.5975	—	—

Table 2: Values of $a_{\max}$ and of Ra_c, for modes with $r=0$, $r=0.5$ and $r=1$, having different values of γ.

reveals that determining the large–time behaviour of the wavepackets just depends on the properties of the dispersion relation,

$$\lambda = \lambda(k). \tag{27}$$

Starting from equations (13) and (15), one can write

$$P_n(x,z,t) = \frac{1}{\sqrt{2\pi}} \int_{-\infty}^{\infty} e^{\lambda(k)t+ikx}\, f(z)\, \mathrm{d}k, \quad \theta_n(x,z,t) = \frac{1}{\sqrt{2\pi}} \int_{-\infty}^{\infty} e^{\lambda(k)t+ikx}\, h(z)\, \mathrm{d}k. \tag{28}$$

At very large times, $t \gg 1$, the absolute value of the integrals in equation (28) can be approximated as [16]

$$|P_n(x,z,t)| \simeq \frac{\mathcal{F}_1(x,z)}{\sqrt{t}}\, e^{\mathrm{Re}(\lambda(k_0))t}, \quad |\theta_n(x,z,t)| \simeq \frac{\mathcal{F}_2(x,z)}{\sqrt{t}}\, e^{\mathrm{Re}(\lambda(k_0))t}. \tag{29}$$

Here, $\mathcal{F}_1(x,z)$ and $\mathcal{F}_2(x,z)$ are functions of (x,z), whose evaluation is not required to assess whether the wavepackets are expected to grow or be damped exponentially for large time. Moreover, k_0 is a saddle point, namely a complex zero of $\lambda'(k)$, that satisfies the holomorphy requirement [16]. In fact, there must exist a continuous deformation of the real axis in the complex k plane which defines a path locally crossing the saddle point k_0 along a line of steepest descent. The holomorphy requirement means that the region in the complex k plane between such path and the real axis does not contain any singular point of the function $\lambda(k)$ [16]. According to equation (29), the linear instability of the wavepacket perturbations arises when

$$\mathrm{Re}(\lambda(k_0)) > 0. \tag{30}$$

Thus, the forthcoming analysis of the absolute instability is entirely grounded on the determination of the saddle points, *i.e.* the roots of $\lambda'(k)=0$, and on the check that they satisfy the holomorphy requirement.

We start from equations (16) with the aim of imposing the saddle point condition, namely $\lambda'(k)=0$. We introduce the functions,

$$\hat{f} = \frac{\partial f}{\partial k}, \qquad \hat{h} = \frac{\partial h}{\partial k}. \tag{31}$$

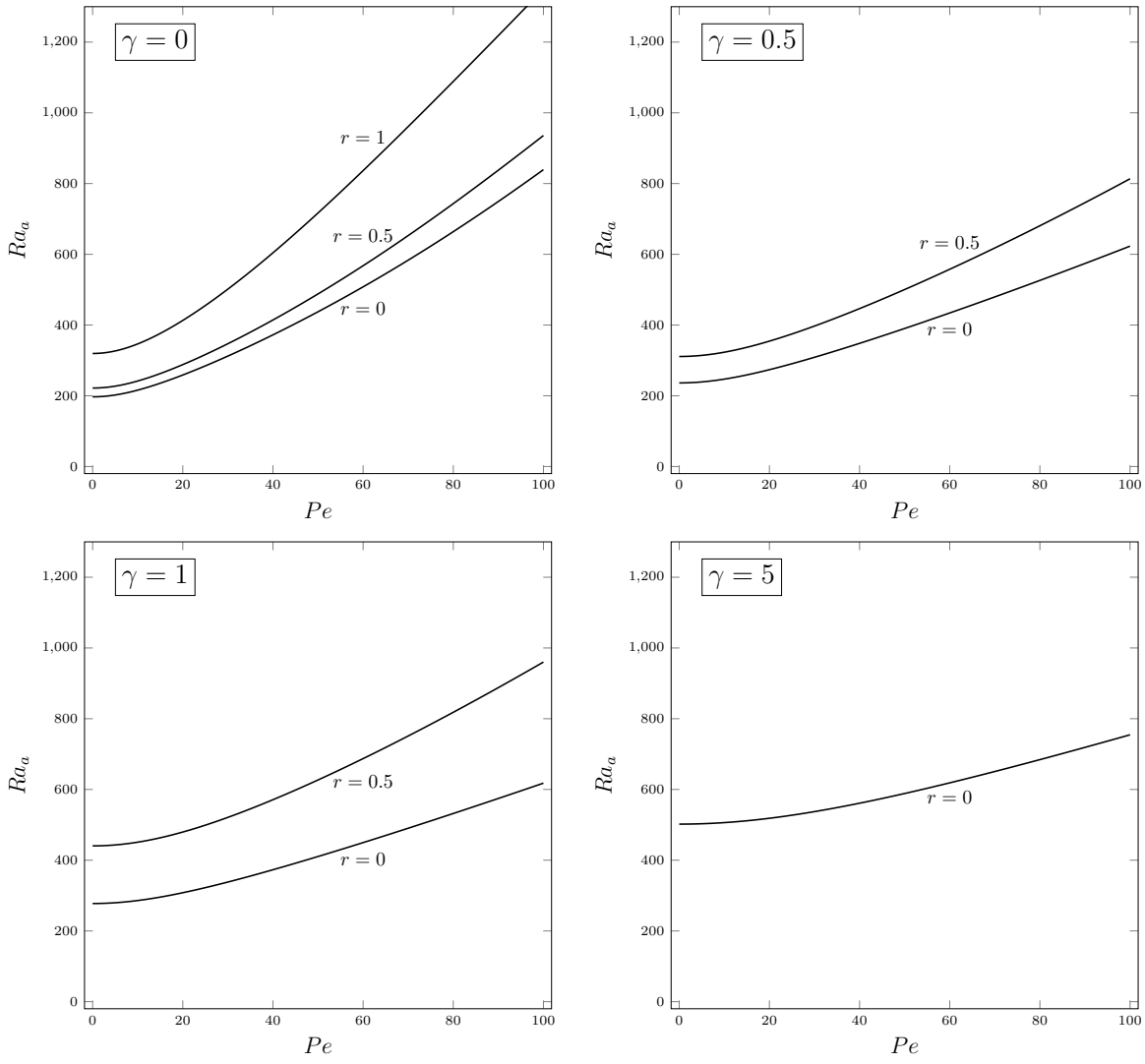

Figure 6: Plots of Ra_a versus Pe for different values of r and γ.

Thus, by deriving all the differential equations and boundary conditions (16) with respect to k, the resulting eigenvalue problem displays a doubled differential order. In fact, by taking into account the condition $\lambda'(k) = 0$, we can write

$$f'' - \left(k^2 + r^2\right) f - i\, k Ra\, h = 0, \tag{32a}$$

$$h'' - \left[k^2 + r^2 + i\, k(Pe + Ra\, x) + \sigma\lambda\right] h + f' = 0, \tag{32b}$$

$$\hat{f}'' - \left(k^2 + r^2\right) \hat{f} - i\, k Ra\, \hat{h} - 2k\, f - i\, Ra\, h = 0, \tag{32c}$$

$$\hat{h}'' - \left[k^2 + r^2 + i\, k(Pe + Ra\, x) + \sigma\lambda\right] \hat{h} + \hat{f}' - [2k + i\,(Pe + Ra\, x)] h = 0, \tag{32d}$$

$$f \pm \gamma\, f' = 0, \quad h = 0, \quad \hat{f} \pm \gamma\, \hat{f}' = 0, \quad \hat{h} = 0 \quad \text{if} \quad x = \pm\frac{1}{2}. \tag{32e}$$

Equations (32) are to be solved by fixing input values of Pe and r, as well as by imposing the

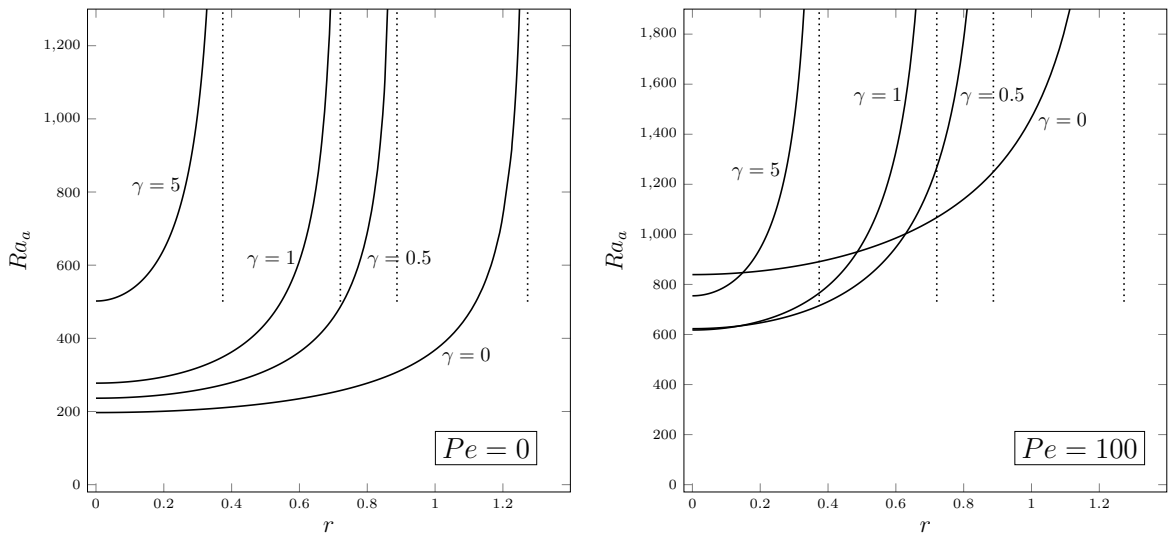

Figure 7: Plots of Ra_a versus r for different values of γ with either $Pe = 0$ or 100. Dotted lines indicate the vertical asymptotes where $r = a_{\max}$.

threshold condition for the onset of absolute instability implied by equation (29), namely $\mathrm{Re}(\lambda(k)) = 0$. Then, equations (32) are solved numerically by employing the same shooting method mentioned for the solution of equations (20). In this case, the output of the eigenvalue problem solution is the list of parameters $(\mathrm{Re}(k), \mathrm{Im}(k), \mathrm{Im}(\sigma\,\lambda), Ra)$. Such an output has a definite meaning as $\mathrm{Re}(k)$ and $\mathrm{Im}(k)$ are the real and imaginary parts of the saddle point k_0, while $Ra = Ra_a$ is the estimated threshold to absolute instability. We say 'estimated threshold' since the evaluated saddle point k_0 needs to be tested for its fulfilment of the holomorphy requirement discussed above. This test can be carried out efficiently for a few sample cases by mapping the isolines of $\mathrm{Re}(\lambda)$ in the complex k plane [16, 19].

6.1. Upflow and downflow

The analysis carried out in Section 5 revealed that the value of Pe does not influence the neutral stability conditions, if not for the value of the angular frequency ω. In fact, since we have noted that the neutral stability condition is accomplished with $\xi = 0$, equation (17) reveals that the neutrally stable value of ω coincides with $k\,Pe/\sigma$.

For the absolute instability, the scenario is different as Pe is expected to influence significantly the threshold value $Ra = Ra_a$. However, inspection of the eigenvalue problem (32) shows that just the absolute value of Pe influences the threshold value Ra_a, but not its sign. In fact, if k_0 is the saddle point evaluated by solving equations (32) and λ the complex eigenvalue obtained with the solution, then applying the change $Pe \to -Pe$ just yields $k_0 \to \bar{k}_0$ and $\lambda \to \bar{\lambda}$, while Ra_a does not change, where overlines denote the complex conjugate. The proof of this result is straightforward. One takes the complex conjugate of the eigenvalue problem (32). Then, the complex conjugate problem can be made identical to (32) provided that one applies the transformation,

$$\bar{f} \to -f, \quad \bar{h} \to h, \quad \bar{\hat{f}} \to -\hat{f}, \quad \bar{\hat{h}} \to \hat{h}, \quad \bar{k} \to k, \quad \sigma\bar{\lambda} \to \sigma\lambda$$

$$r \to r, \quad Pe \to -Pe, \quad Ra \to Ra, \quad \gamma \to \gamma, \quad x \to -x. \tag{33}$$

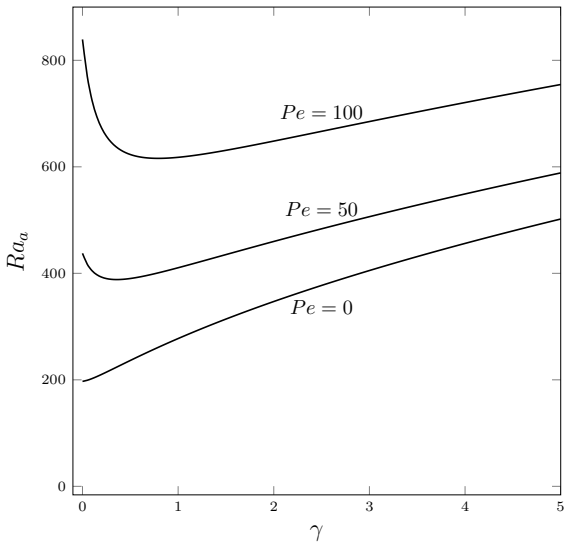

Figure 8: Plots of Ra_a versus γ for different values of Pe and $r = 0$.

As a consequence, one can restrict our forthcoming analysis to $Pe > 0$, having in mind that Ra_a does not change by changing the sign of Pe, while k_0 and λ are obtained by complex conjugation. Physically, the symmetry defined by equation (33) implies a simple relation between the onset of absolute instability for upflows ($Pe > 0$) and downflows ($Pe < 0$).

6.2. Evaluation of the threshold Ra_a to absolute instability

Figure 6 displays plots of Ra_a versus Pe for different values of γ and $r = 0, 0.5$ and 1. We recall that, for every prescribed γ, instability is possible only with modes having $r \leq a_{\max}$. For the values of γ considered in Fig. 6, the values of $a_{\max}$ are provided in Table 2. This is the reason why we took $r = 0, 0.5$ and 1 with $\gamma = 0$, $r = 0$ and 0.5 with $\gamma = 0.5$ and 1, while we considered only $r = 0$ with $\gamma = 5$. Figure 6 suggests that $r = 0$ is the most unstable situation yielding the transition to absolute instability. This means that, whatever is the finite aspect ratio s, the y independent modes with $n = 0$ are those triggering the transition to the absolute instability. This feature is coherent with what we inferred in section 5 on studying the modal instability. When $Pe = 0$, the transition to absolute instability occurs at the onset of modal instability, namely $Ra_a = Ra_c$, where the values of Ra_c are those reported in Table 2 for all the cases examined in Fig. 6. This is the usual behaviour, which is physically reasonable as the vertical net flow parametrised by Pe is the cause of the delayed transition to absolute instability relative to the onset of modal instability. Another important phenomenon displayed in Fig. 6 is that the transition to absolute instability happens with a Rayleigh number Ra_a which monotonically increases with Pe. However, the influence of the increasing Pe becomes weaker as the permeability parameter γ increases. Thus, if Ra_a increases with γ for $Pe = 0$, we report a higher value of Ra_a for $\gamma = 0$ than for $\gamma = 0.5$, 1 or 5, when $Pe = 100$.

Evidence that the modes $r = 0$ are those leading the transition to absolute instability is provided by Fig. 7. This figure shows that Ra_a monotonically increases with r and, for every given value of γ, it approaches the vertical asymptote $r = a_{\max}$. Figure 7 involves just the cases $Pe = 0$ and $Pe = 100$, but the same conclusion can be gained with other values of Pe. We recall that, when

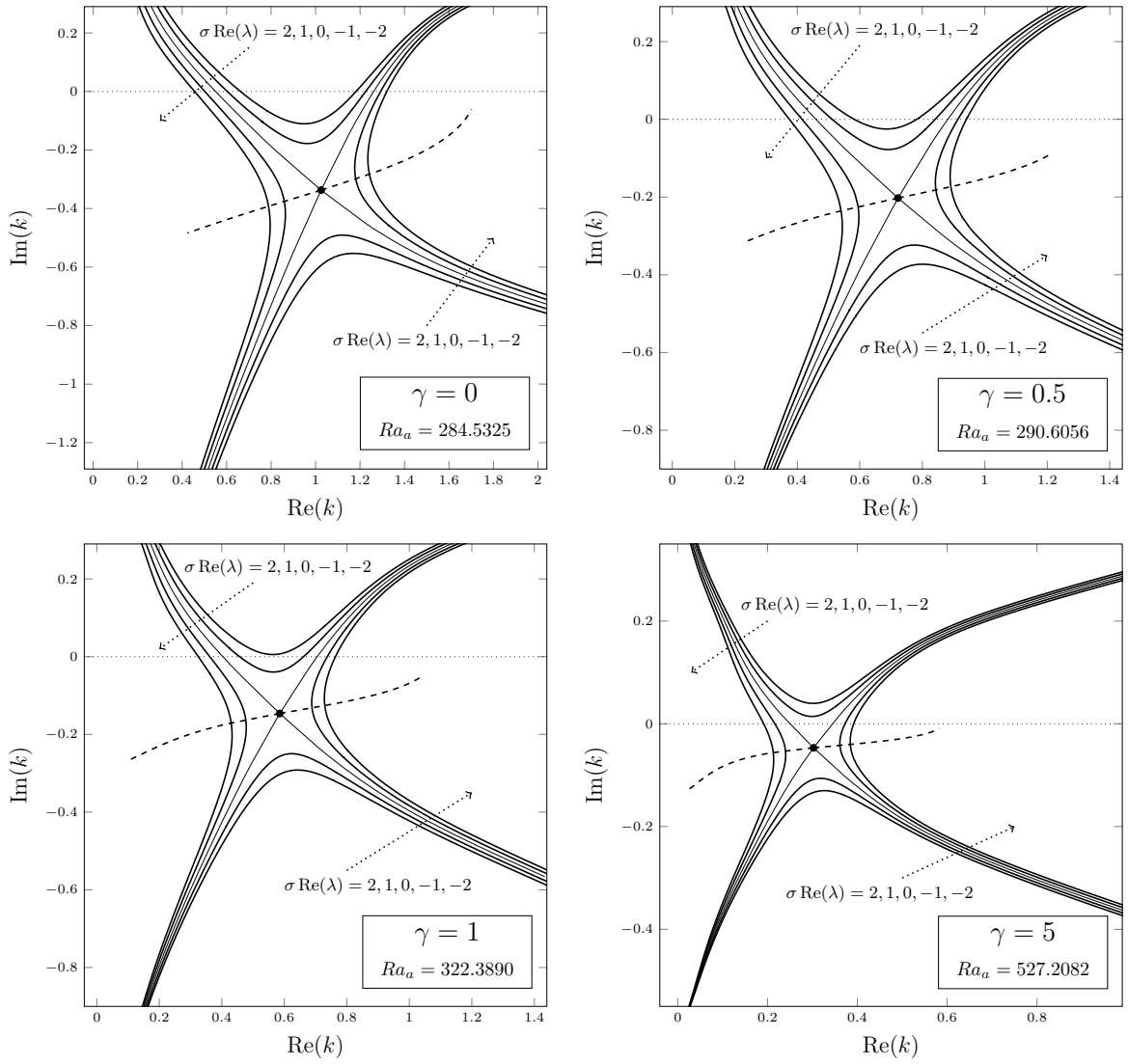

Figure 9: Isolines of $\mathrm{Re}(\lambda)$ in the complex k plane for $Pe = 25$, $Ra = Ra_a$, $r = 0$ and different values of γ; thin solid lines are for $\mathrm{Re}(\lambda) = 0$, while $\mathrm{Re}(\lambda) = \pm 1$ and ± 2 are the thick solid lines; the thick dashed lines are, for each γ, the paths of steepest descent crossing the saddle points denoted as black dots.

$Pe = 0$, we have $Ra_a = Ra_c$. Then, the frame of Fig. 7 relative to $Pe = 0$ provides an illustration of the property described in Section 5, namely that the modal instability occurs with $r = 0$ at its onset. Again, the non–monotonic dependence on γ, already discussed with reference to Fig. 6, is exploited also by the data reported in Fig. 7 for $Pe = 100$. A focus on this phenomenon is provided with Fig. 8. In this figure, the change from a monotonic dependence on γ, displayed with $Pe = 0$, to a non–monotonic behaviour with a minimum attained with $\gamma > 0$, displayed for both $Pe = 50$ and 100, is shown. Reference is made to the modes having $r = 0$ as we have already concluded that they provide the lowest transition to absolute instability.

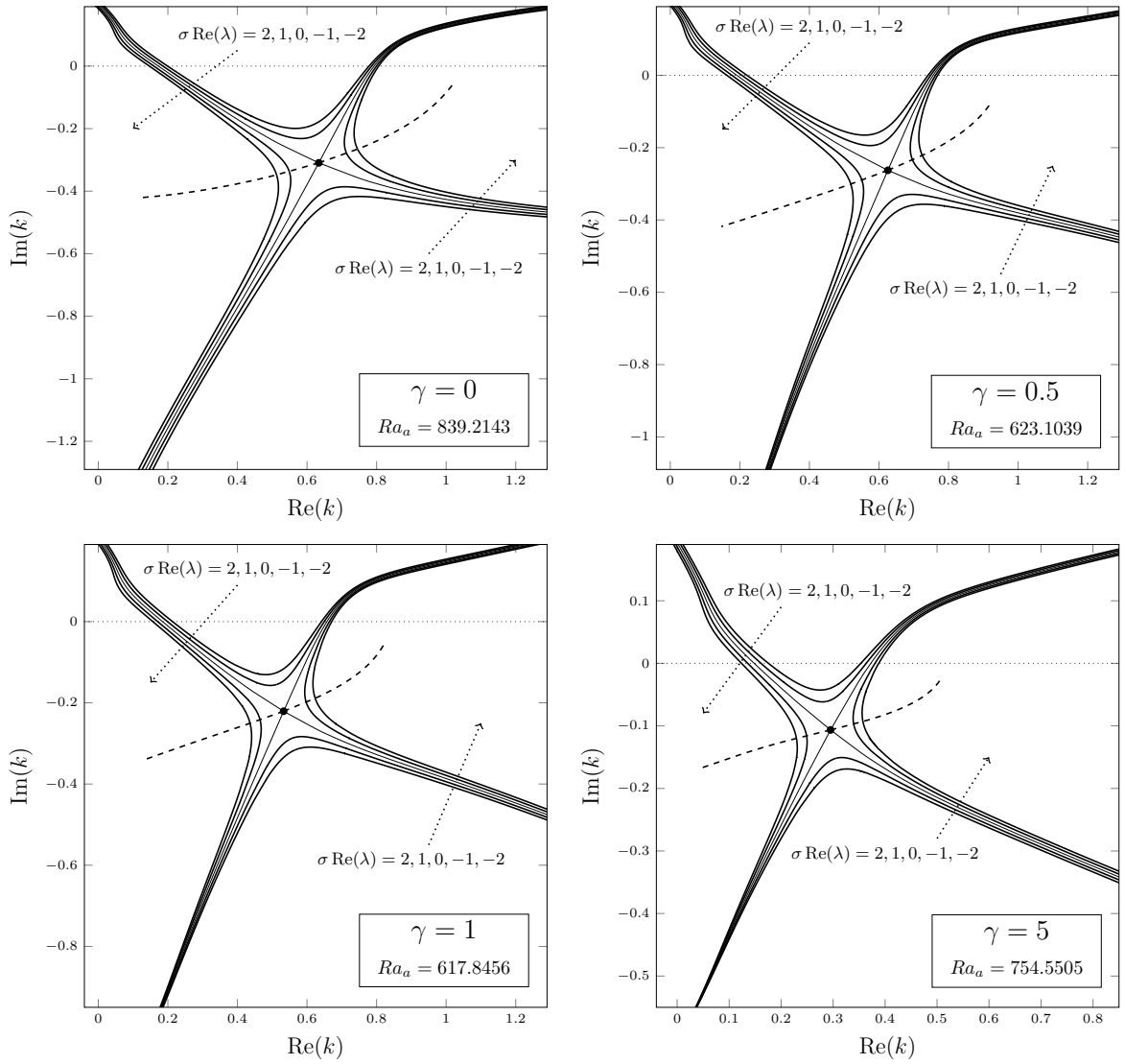

Figure 10: Isolines of $\mathrm{Re}(\lambda)$ in the complex k plane for $Pe = 100$, $Ra = Ra_a$, $r = 0$ and different values of γ; thin solid lines are for $\mathrm{Re}(\lambda) = 0$, while $\mathrm{Re}(\lambda) = \pm 1$ and ± 2 are the thick solid lines; the thick dashed lines are, for each γ, the paths of steepest descent crossing the saddle points denoted as black dots.

6.3. The holomorphy requirement

The steepest descent approximation of the Fourier integrals, such as those defined by equation (28), requires that one can deform the integration through the real axis to a contour crossing the saddle point k_0, locally, along a path of steepest descent. The deformation ought to be continuous, meaning that no singularity of $\lambda(k)$ can be trapped between the deformed path in the complex k plane and the real axis [16, 36]. In principle, one should verify that the holomorphy requirement is satisfied for every assigned set of input parameters (r, γ, Pe). However, this test is virtually impractical as one should check the form of the isolines of $\mathrm{Re}(\lambda)$ in every case examined. Then, the usual approach is to discuss a few sample cases assuming that they are illustrative of the

	$Pe = 25$		$Pe = 100$	
γ	k_0	$\sigma\,\mathrm{Im}(\lambda)$	k_0	$\sigma\,\mathrm{Im}(\lambda)$
0	$1.024907 - 0.3370352\,i$	-24.23909	$0.6338261 - 0.3094949\,i$	-55.87563
0.5	$0.7223700 - 0.2026787\,i$	-17.45752	$0.6254681 - 0.2625933\,i$	-55.46861
1	$0.5854439 - 0.1462960\,i$	-14.27211	$0.5328108 - 0.2206786\,i$	-48.17387
5	$0.3025419 - 0.04674883\,i$	-7.495872	$0.2951300 - 0.1064626\,i$	-27.94600

Table 3: Saddle points k_0 and values of $\sigma\,\mathrm{Im}(\lambda)$ at transition to absolute instability with $r = 0$ and for different Pe and γ.

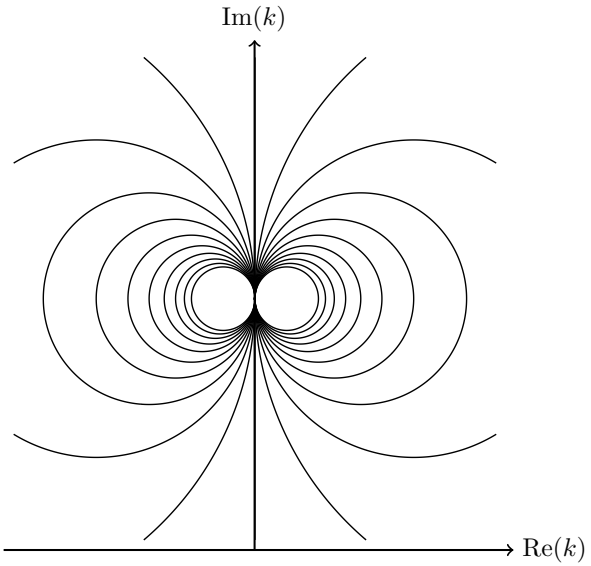

Figure 11: A qualitative sketch of a simple pole singularity in the complex k plane drawn through the isolines of the real part of $\lambda(k)$.

general behaviour [16, 22, 37, 38].

An important feature of the stability eigenvalue problem (16) is its symmetry under the transformation

$$k \to -\bar{k}. \tag{34}$$

Then, we can just focus our attention on the half–plane $\mathrm{Re}(k) > 0$ as the form of the isolines of $\mathrm{Re}(\lambda)$ in the region $\mathrm{Re}(k) < 0$ can be obtained by a simple mirror reflection [16]. Furthermore, every saddle point k_0 in the region $\mathrm{Re}(k) > 0$ has a mirror twin, namely $-\bar{k}_0$, with the same imaginary part and a negative real part.

We have already pointed out that the transition to absolute instability is activated by the $r = 0$ modes. Thus, our check of the holomorphy requirement will be restricted to the case $r = 0$. Two values of the Péclet number will be considered: 25 and 100. For each value of Pe, the dependence on γ has been tested by assuming the values: 0, 0.5, 1 and 5. Figures 9 and 10 illustrate the test cases $Pe = 25$ and $Pe = 100$, respectively. Each frame of Figs. 9 and 10 is relative to a given γ and displays isolines of $\mathrm{Re}(\lambda)$ in the complex k plane. Such isolines are drawn for the Rayleigh number Ra_a defining the transition to absolute instability with the given values of Pe, γ and $r = 0$.

The $\mathrm{Re}(\lambda) = constant$ patterns are displayed around the saddle point triggering the transition to absolute instability and, thus, placed at the intersection of the $\mathrm{Re}(\lambda) = 0$ lines. The path of steepest descent, identified as a thick dashed line crossing the saddle point, is an isoline of $\mathrm{Im}(\lambda)$ as explained, for instance, in the book by Barletta [16]. The values of $\sigma\,\mathrm{Im}(\lambda)$ for the saddle points are those evaluated numerically by solving equations (32). Table 3 reports such values for the cases involved in Figs. 9 and 10. The shape of the isolines drawn in Figs. 9 and 10 illustrates the absence of singularities of the complex valued function $\lambda(k)$ in the region between the deformed path matching the line of steepest descent close to the saddle point and the real k axis. In fact, a pole singularity is easily detected in the complex k plane as it would have the form of an attraction point for the isolines with all possible values of $\mathrm{Re}(\lambda)$ [16, 19, 36]. This elementary behaviour is depicted qualitatively in Fig. 11. All these considerations lead us to establish that the determined thresholds to absolute instability, as obtained through the solution of the eigenvalue problem (32), are coherent with the steepest–descent approximation of Fourier integrals.

7. Comparison with an experiment

Even though, to date and to the best of the authors' knowledge, there are no available experimental data regarding cases with $Pe \neq 0$, an interesting comparison with measurements relative to the onset of convective rolls performed for a vertical porous slab in a basic state with a vanishing flow rate is possible. In fact, Kwok and Chen [39] carried out an experiment involving a tall, narrow vertical layer, 30 cm high $\times$ 2 cm wide $\times$ 11.5 cm deep, of glass beads saturated by distilled water. The authors reported a phenomenon of convection heat transfer whose onset was evaluated at a critical Rayleigh number equal to 66.2. Such an experimental outcome turned out to be utterly in contrast with the conclusions drawn in the paper by Gill [1] as his theorem predicted no possible onset of convection cells. Then, Kwok and Chen [39] provided two possible explanations for the strong discrepancy between theory and experiments: the importance of Brinkman's term in the momentum balance, whereas such a term was neglected in Gill's analysis [1]; the importance of variable water viscosity effects. Kwok and Chen [39] numerically evaluated the expected critical Rayleigh number by taking into account Brinkman's term with constant viscosity and obtained 308, while by taking into account the effects of variable viscosity without Brinkman's term they obtained 98.3. The former value is significantly larger than the experimental datum, 66.2. Moreover, the porosity of the glass beads layer measured by Kwok and Chen [39] is 0.40. Thus, it looks a bit too small to justify an important effect of Brinkman's term (Nield and Bejan [23] suggest that Brinkman's term should be taken into account only if the porosity is larger than 0.6). On the other hand, the variable viscosity contribution to the momentum balance looks realistic, even if it yields a critical Rayleigh number which is larger than the measured value.

Our analysis may contribute significantly to the comparisons between theory and experiments. In fact, by neglecting both Brinkman's term and the temperature–dependence of the fluid viscosity, we predict a critical Rayleigh number for the onset of the instability which, as reported by equation (24), can be as small as 197. This value is larger than the experimental datum determined by Kwok and Chen [39], but it suggests that the impermeability conditions for the boundaries assumed both by Gill [1] and by Kwok and Chen [39] may not be the best model for the actual experimental setup. Trying to envisage new paths for future research, it is possible that a theoretical model where partial permeability of the layer boundaries and variable viscosity of the fluid are accounted for may be a good candidate for a fair comparison between theory and experiments. Another important element which may justify the discrepancy between the actual theoretical predictions

and experimental data is the possible subcritical nature of the instability. Straughan [4] ruled out the possibility of a subcritical instability for a vertical porous layer, but his study is based on the assumption of a porous layer with impermeable boundaries. No study of the nonlinear, possibly subcritical, instability has yet been carried out by relaxing the boundary conditions from impermeability to a model of partial permeability.

8. Conclusions

The buoyant flow in a vertical porous slab saturated by a fluid and bounded by parallel permeable planes at different uniform temperatures is investigated. The stability of the basic parallel flow has been tested versus perturbations expressed as single Fourier modes, as well as versus localised wavepacket perturbations. The former test leads us to the neutral stability condition for the onset of the modal instability, while the latter test leads us to the identification of the threshold to absolute instability. Different Fourier modes of perturbations are identified by the pair (r, k), where r is a positive parameter which depends on the spanwise confinement of the porous slab, while k is the wavenumber in the vertical direction. The order parameter for the transition to the instability is the Rayleigh number, Ra, for the saturated porous medium. Other dimensionless parameters influencing the onset of the instability are the Péclet number, proportional to the vertical flow rate, and the parameter γ tuning the permeability of the vertical plane boundaries, where $\gamma = 0$ means perfect permeability and $\gamma \to \infty$ means impermeability. The eigenvalue problem for the linear stability analysis has been solved leading to the identification of the transition conditions to the modal instability and to the absolute instability. The main results obtained with this study can be outlined as follows:

- The onset of the modal instability occurs via $r = 0$ modes, namely Fourier modes independent of the spanwise coordinate y. The Péclet number does not influence the neutral stability curves displayed in the (k, Ra) plane. The neutral stability condition involves larger and larger Rayleigh numbers as γ increases. Eventually, when $\gamma \to \infty$ the numerical data support the result rigorously proved by Gill [1]: the slab with impermeable boundaries yields no instability. Hence, an increasing γ stabilises the basic flow.

- The threshold value of Ra for the transition to absolute instability, *i.e.* Ra_a, is an increasing function of Pe. Physically, the larger is the vertical flow rate in the porous slab the harder is the destabilization from a localised wavepacket disturbance. Here, harder means that larger and larger temperature differences between the boundaries are needed for the flow to become absolutely unstable.

- The transition to absolute instability is activated by the $r = 0$, or y independent, Fourier modes. The dependence of Ra_a on the permeability parameter γ may be non–monotonic for $Pe > 0$, this phenomenon has been illustrated for $Pe = 50$ and 100.

- The consistency of the steepest–descent approximation of the wavepackets at large times has been checked by drawing the isolines of the complex–valued growth rate in the complex k plane. The holomorphy requirement turned out to be satisfied in all the test cases considered, involving either $Pe = 25$ or $Pe = 100$.

Much more can be done in the future to further explore these topics. In particular, the development of a nonlinear analysis of the instability is quite interesting both to inspect the possible onset of

subcritical instability or to evaluate the heat transfer rate at supercritical conditions. Moreover, one may aim to shed some light on the influence of the nonlinearity on the emergence of the absolute instability.

Acknowledgements

The authors A. Barletta and M. Celli acknowledge the financial support from the grant PRIN 2017F7KZWS provided by the Italian Ministry of Education and Scientific Research.

References

[1] A. E. Gill, A proof that convection in a porous vertical slab is stable, Journal of Fluid Mechanics 35 (1969) 545–547.

[2] C. M. Vest, V. S. Arpaci, Stability of natural convection in a vertical slot, Journal of Fluid Mechanics 36 (1969) 1–15.

[3] D. A. S. Rees, The stability of Prandtl-Darcy convection in a vertical porous layer, International Journal of Heat and Mass Transfer 31 (1988) 1529–1534.

[4] B. Straughan, A nonlinear analysis of convection in a porous vertical slab, Geophysical & Astrophysical Fluid Dynamics 42 (1988) 269–275.

[5] S. Lewis, A. P. Bassom, D. A. S. Rees, The stability of vertical thermal boundary-layer flow in a porous medium, European Journal of Mechanics B Fluids 14 (1995) 395–407.

[6] D. A. S. Rees, J. L. Lage, The effect of thermal stratification on natural convection in a vertical porous insulation layer, International Journal of Heat and Mass Transfer 40 (1996) 111–121.

[7] D. A. S. Rees, The effect of local thermal nonequilibrium on the stability of convection in a vertical porous channel, Transport in Porous Media 87 (2011) 459–464.

[8] N. L. Scott, B. Straughan, A nonlinear stability analysis of convection in a porous vertical channel including local thermal nonequilibrium, Journal of Mathematical Fluid Mechanics 15 (2013) 171–178.

[9] A. Barletta, A proof that convection in a porous vertical slab may be unstable, Journal of Fluid Mechanics 770 (2015) 273–288.

[10] A. Barletta, Instability of stationary two-dimensional mixed convection across a vertical porous layer, Physics of Fluids 28 (2016) 014101.

[11] A. Barletta, M. Celli, M. N. Ouarzazi, Unstable buoyant flow in a vertical porous layer with convective boundary conditions, International Journal of Thermal Sciences 120 (2017) 427–436.

[12] M. Celli, A. Barletta, D. A. S. Rees, Local thermal non-equilibrium analysis of the instability in a vertical porous slab with permeable sidewalls, Transport in Porous Media 119 (2017) 539–553.

[13] A. Barletta, D. A. S. Rees, On the onset of convection in a highly permeable vertical porous layer with open boundaries, Physics of Fluids 31 (2019) 074106.

[14] P. G. Drazin, W. H. Reid, Hydrodynamic Stability, Cambridge University Press, Cambridge, UK, 2004.

[15] P. J. Schmid, D. S. Henningson, Stability and Transition in Shear Flows, Springer, New York, 2012.

[16] A. Barletta, Routes to Absolute Instability in Porous Media, Springer, New York, NY, 2019.

[17] P. Huerre, P. A. Monkewitz, Absolute and convective instabilities in free shear layers, Journal of Fluid Mechanics 159 (1985) 151–168.

[18] P. Huerre, On the absolute/convective nature of primary and secondary instabilities, in: J. E. Wesfreid, H. R. Brand, P. Manneville, G. Albinet, N. Boccara (Eds.), Propagation in Systems Far from Equilibrium, Springer, Berlin, 1988, pp. 340–353.

[19] M. P. Juniper, A. Hanifi, V. Theofilis, Modal stability theory, Applied Mechanics Reviews 66 (2014) 024804.

[20] A. Barletta, L. S. de B. Alves, Absolute instability: A toy model and an application to the Rayleigh-Bénard problem with horizontal flow in porous media, International Journal of Heat and Mass Transfer 104 (2017) 438–455.

[21] A. Barletta, M. Celli, Convective to absolute instability transition in a horizontal porous channel with open upper boundary, Fluids 2 (2017) 33.

[22] L. S. de B. Alves, S. C. Hirata, M. Schuabb, A. Barletta, Identifying linear absolute instabilities from differential eigenvalue problems using sensitivity analysis, Journal of Fluid Mechanics 870 (2019) 941–969.

[23] D. A. Nield, A. Bejan, Convection in Porous Media, Springer, New York, 5th edition, 2017.

[24] B. K. Hartline, C. R. B. Lister, Thermal convection in a Hele–Shaw cell, Journal of Fluid Mechanics 79 (1977) 379–389.

[25] C. R. B. Lister, An explanation for the multivalued heat transport found experimentally for convection in a porous medium, Journal of Fluid Mechanics 214 (1990) 287–320.

[26] C. W. Horton, F. T. Rogers, Convection currents in a porous medium, Journal of Applied Physics 16 (1945) 367–370.

[27] E. R. Lapwood, Convection of a fluid in a porous medium, Proceedings of the Cambridge Philosophical Society 44 (1948) 508–521.

[28] F. W. Crawford, J. A. Tataronis, Absolute instabilities of perpendicularly propagating cyclotron harmonic plasma waves, Journal of Applied Physics 36 (1965) 2930–2934.

[29] C. Beasley, J. Cordey, Convective and absolute ion cyclotron instabilities in homogeneous plasmas, Plasma Physics 10 (1968) 411–419.

[30] P. Huerre, Spatio–temporal instabilities in closed and open flows, in: E. Tirapegui, D. Villarroel (Eds.), Instabilities and Nonequilibrium Structures, Springer, Berlin, 1987, pp. 141–177.

[31] P. A. Monkewitz, D. W. Becherte, B. Barsikow, B. Lehmann, Experiments on the absolute instability of heated jets, in: H.-H. Fernholz, H. E. Fiedler (Eds.), Advances in Turbulence 2, Springer, Berlin, 1989, pp. 455–460.

[32] R. J. Lingwood, An experimental study of absolute instability of the rotating–disk boundary–layer flow, Journal of Fluid Mechanics 314 (1996) 373–405.

[33] A. Delache, M. N. Ouarzazi, M. Combarnous, Spatio–temporal stability analysis of mixed convection flows in porous media heated from below: comparison with experiments, International Journal of Heat and Mass Transfer 50 (2007) 1485–1499.

[34] H. S. Nygård, P. A. Tyvand, Onset of convection in a porous box with partly conducting and partly penetrative sidewalls, Transport in Porous Media 84 (2010) 55–73.

[35] B. Straughan, Stability and Wave Motion in Porous Media, Springer, New York, NY, 2008.

[36] M. J. Ablowitz, A. S. Fokas, Complex Variables: Introduction and Applications, Cambridge University Press, Cambridge, UK, 2003.

[37] M. Schuabb, L. S. de B. Alves, S. Hirata, Two- and three-dimensional absolute instabilities in a porous medium with inclined temperature gradient and vertical throughflow, Transport in Porous Media 132 (2020) 135–155.

[38] A. Barletta, M. Celli, P. V. Brandão, L. S. de B. Alves, Wavepacket instability in a rectangular porous channel uniformly heated from below, International Journal of Heat and Mass Transfer 147 (2020) 118993.

[39] L. P. Kwok, C. F. Chen, Stability of thermal convection in a vertical porous layer, ASME Journal of Heat Transfer 109 (1987) 889–893.

Appendix A. Pressure boundary conditions

The pressure conditions describing an imperfectly permeable boundary given by a vertical plane is based on Darcy's law with the pressure drop driving the seepage flow across the boundary is the difference between the boundary pressure and the external environment pressure. As this difference is evaluated at a fixed vertical quota, it coincides with $p - p_{\text{ext}}$, where we consider the dynamic pressure (the local difference between the pressure and the hydrostatic pressure) instead of the pressure. Thus, we can write,

$$\frac{\mu}{K}\,\mathbf{u}\cdot\hat{\mathbf{e}}_n = G\,(p - p_{\text{ext}})\,, \tag{A.1}$$

where $\hat{\mathbf{e}}_n$ is the outward normal to the boundary plane and G is a momentum transfer coefficient with the dimensions of an inverse length. By employing Darcy's law to express $\mathbf{u}\cdot\hat{\mathbf{e}}_n$ at the boundary,

$$\frac{\mu}{K}\,\mathbf{u}\cdot\hat{\mathbf{e}}_n = -\boldsymbol{\nabla} p\cdot\hat{\mathbf{e}}_n. \tag{A.2}$$

By combining equations (A.1) and (A.2), we obtain

$$\boldsymbol{\nabla} p \cdot \hat{\mathbf{e}}_n + G\,(p - p_{\text{ext}}) = 0, \tag{A.3}$$

which, in a dimensionless form obtained by means of the scaling defined in equation (1), can be rewritten as

$$p + \gamma\, \boldsymbol{\nabla} p \cdot \hat{\mathbf{e}}_n = p_{\text{ext}}. \tag{A.4}$$

Here, the dimensionless parameter γ is defined as

$$\gamma = \frac{1}{G\,L}. \tag{A.5}$$